Science Advances
AAAS

Supplementary Materials for

Structural insights into crista junction formation by the Mic60-Mic19 complex

Tobias Bock-Bierbaum *et al.*

Corresponding author: Oliver Daumke, oliver.daumke@mdc-berlin.de;
Martin van der Laan, martin.van-der-laan@uks.eu

Sci. Adv. **8**, eabo4946 (2022)
DOI: 10.1126/sciadv.abo4946

The PDF file includes:

Other Supplementary Material for this manuscript includes the following:

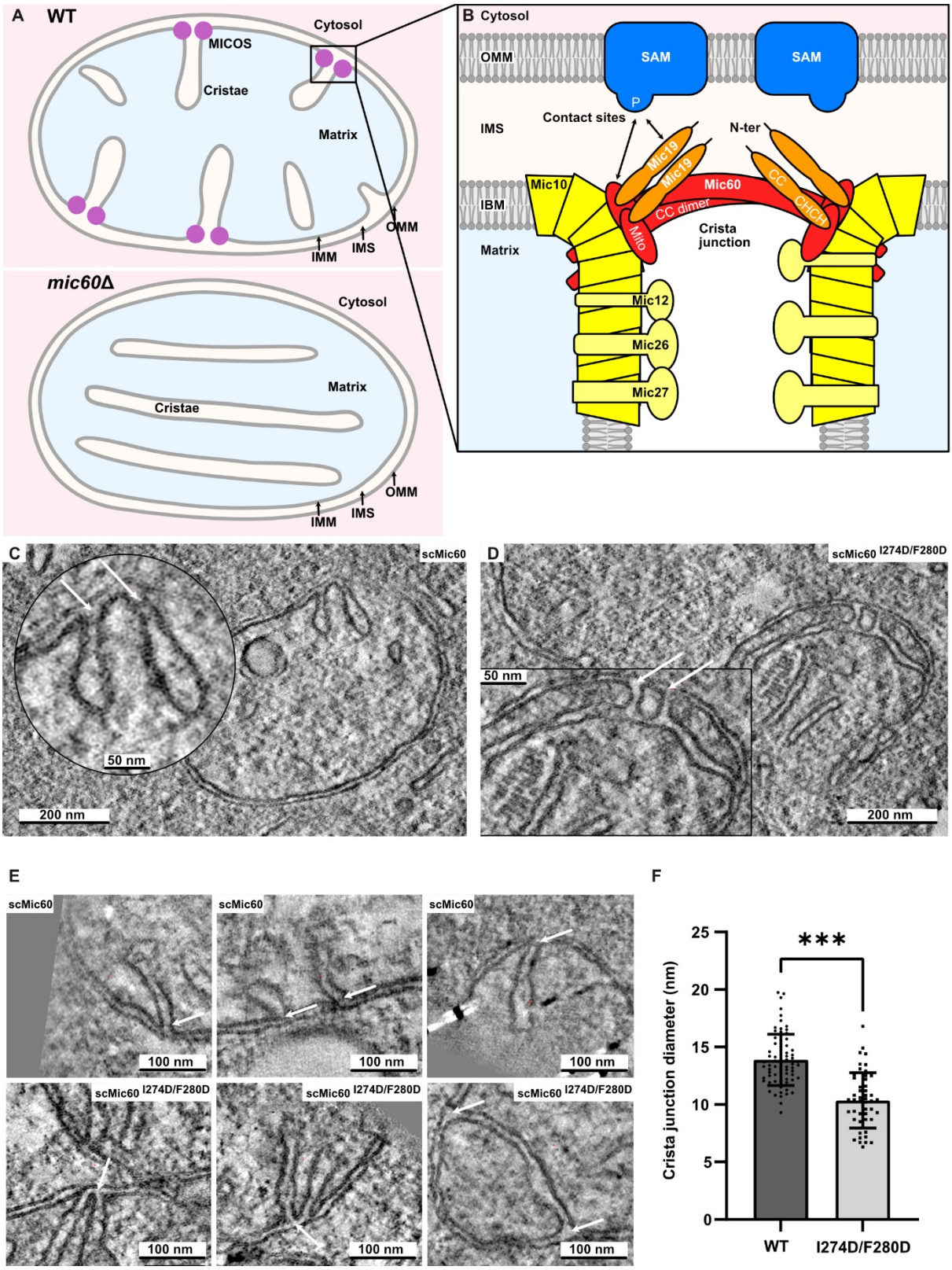

Fig. S1. Overview of mitochondrial architecture

Fig. S1. Overview of mitochondrial architecture

(A) Mitochondria are surrounded by two membrane systems. The outer mitochondrial membrane (OMM) envelopes the organelles and mediates communication and exchange of molecules with the cytosol and other membrane-bound intracellular compartments. The inner mitochondrial membrane (IMM) consists of two structurally and functionally distinct domains. The inner boundary membrane (IBM) is in close proximity to the OMM, comprising the aqueous intermembrane space (IMS) compartment. Large membrane areas, termed cristae, extend from the IMM and wrinkle into the matrix. These cristae membranes adopt the shape of branched tubules, sheets or discs and determine the characteristic ultrastructure of mitochondria. IBM and cristae membranes largely differ in their protein content. Whereas the IBM particularly contains metabolite carriers and translocation machineries for macromolecules, like polypeptides, cristae membranes are exceptionally protein-rich and harbor the respiratory chain complexes and the F_1F_o-ATP synthase for oxidative phosphorylation. The connections between cristae and IBM are termed crista junctions (CJs). These specialized membrane regions exhibit an exceedingly high curvature and are thought to act as diffusion barriers for metabolites and proteins. **(B)** The formation and stabilization of CJs is mediated by an evolutionary conserved hetero-oligomeric protein complex, the mitochondrial contact site and cristae organizing system (MICOS). The core complex consists of six subunits in yeast and seven in metazoa. MICOS is made of a Mic60 and a Mic10 module with distinct properties and functions. Mic60 (formerly known as mitofilin, IMMT, Aim28 or Fcj1) is the centerpiece of the membrane-bridging subcomplex that forms contact sites between IMM and OMM through interactions with partner protein complexes, like the sorting and assembly machinery (SAM). The Mic60 protein consists of an N-terminal transmembrane segment anchored in the IMM and a large hydrophilic domain in the IMS that exhibits an extended coiled-coil region and a C-terminal mitofilin signature domain. Mic60 is firmly associated with Mic19, a peripheral membrane protein that may act as a redox sensor through an intramolecular disulfide bond. In metazoa, the Mic60 module additionally contains Mic25 that belongs to the same protein family as Mic19. Studies in yeast and human mitochondria suggest that the N-terminal domain of Mic19 and parts of the Mic60 IMS domain differentially contribute to membrane contact site formation together with the polypeptide transport-associated (POTRA) domain of Sam50. Homo-oligomers of Mic10 form the backbone structure of the second MICOS subcomplex and contribute to the formation and stabilization of membrane curvature at CJs. The oligomeric state of Mic10 is regulated by Mic26 and Mic27 in an antagonistic manner and modulated by the IMM phospholipid cardiolipin. The two MICOS modules are connected by Mic12 in yeast or Mic13/QIL1 in metazoa. P: POTRA domain of Sam50, N-ter. Mic19: N-terminal region of Mic19, CC: coiled-coil domains, CHCH: coiled-coil-helix-coiled-coil-helix domain, Mito: mitofilin domain, CC dimer: Mic60 coiled-coil domain dimer. Ablation of MICOS leads to the collapse of CJs and the detachment of cristae from the IBM **(A**, **bottom)**. Cristae accumulate as lamellar membrane stacks in the matrix. MICOS-deficient mitochondria show defects in oxidative phosphorylation and a variety of stress responses. **(C)** Representative EM micrograph of mitochondria from fixed *mic60Δ S. cerevisiae* cells reconstituted with plasmid-borne Mic60. Filamentous densities near the CJs are indicated by white arrows. **(D)** Same as in **C**, but reconstituted with the tetramerization mutant $Mic60^{I274D/F280D}$. Interference with Mic60 tetramerization results in a reduction of CJs. **(E) and (F)** Additional EM micrographs (as in **C** and **D**) and quantitative analysis of CJ diameter of mitochondria from fixed *mic60Δ S. cerevisiae* reconstituted with Mic60 (n = 74, mean diameter 13.8 nm) and with the tetramerization variant $Mic60^{I274D/F280D}$ (n = 50, mean diameter 10.4 nm).

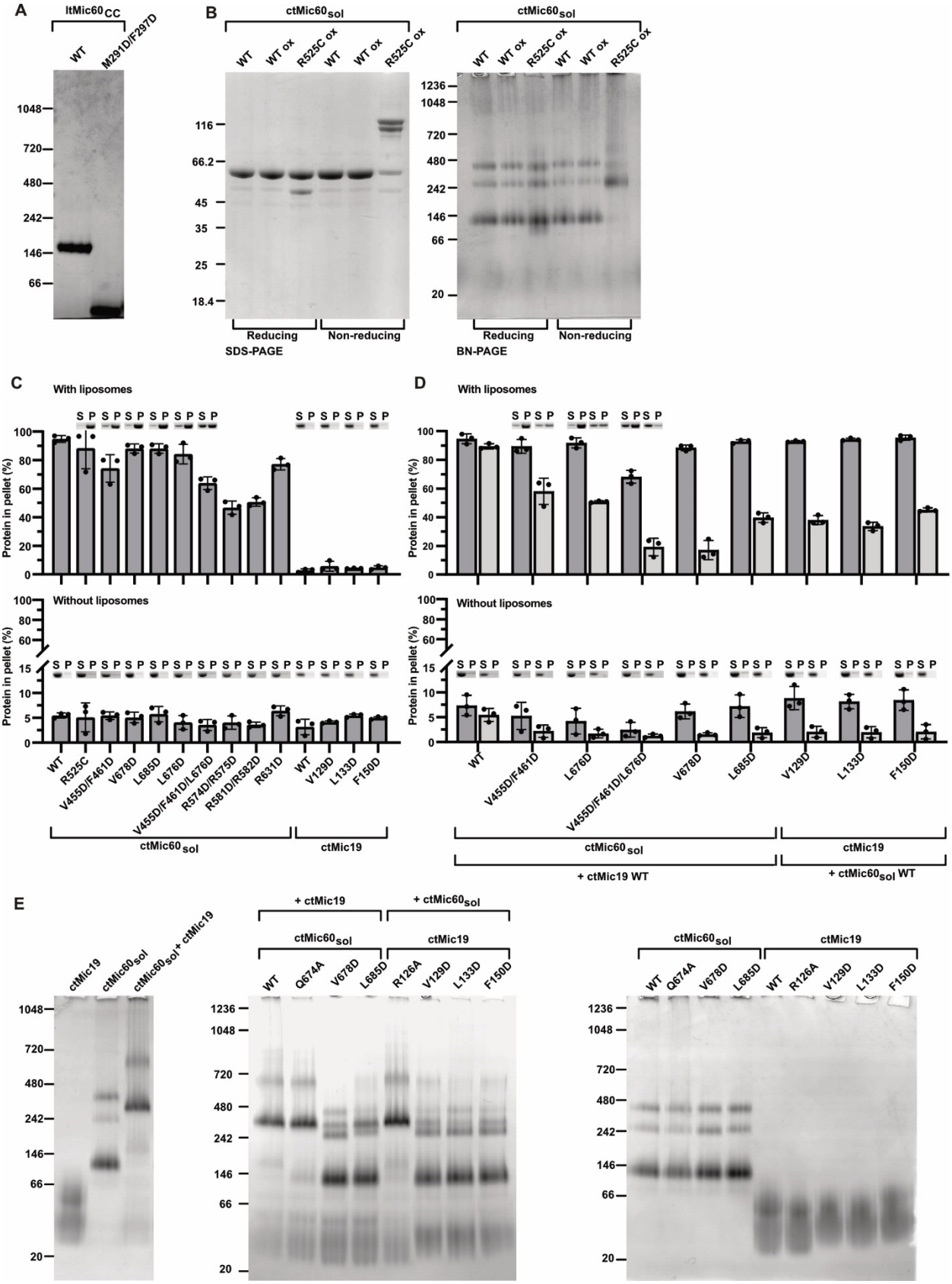

Fig. S2. Oligomerization and interaction of Mic60 and Mic19

Fig. S2. Oligomerization and interaction of Mic60 and Mic19

(A) BN-PAGE analysis of purified ltMic60$_{CC}$ and the tetramerization variant M291D/F297D. **(B)** SDS-PAGE (left) and BN-PAGE (right) analysis of the ctMic60$_{sol}$ and ctMic60$_{sol}^{R525C}$ under reducing and non-reducing conditions. 'WT' represents ctMic60$_{sol}$ under non-oxidized conditions, whereas the lanes 'WT ox' and 'R525C ox' show ctMic60$_{sol}$ and the R525C variant, respectively, after oxidation using $CuSO_4$. **(C), (D)** SDS-PAGE analysis and quantification of liposome co-sedimentation assay using different ctMic60$_{sol}$/ctMic19 single amino acid substitution variants **(C)** and their respective complexes **(D)**. S, supernatant; P, pellet. The light grey bars in **(D)** represent ctMic19 and its variants and the dark grey bars ctMic60$_{sol}$ and its variants. Measurements were done in triplicate and error bars indicate the s.d. of each data set. SDS-PAGE data shown in the main Figs. 3C and 4E are not included here. **(E)** BN-PAGE analysis of ctMic60$_{sol}$ variants and their complexes with ctMic19 variants. Proteins and protein complexes in all figures were visualized with Coomassie Brilliant Blue.

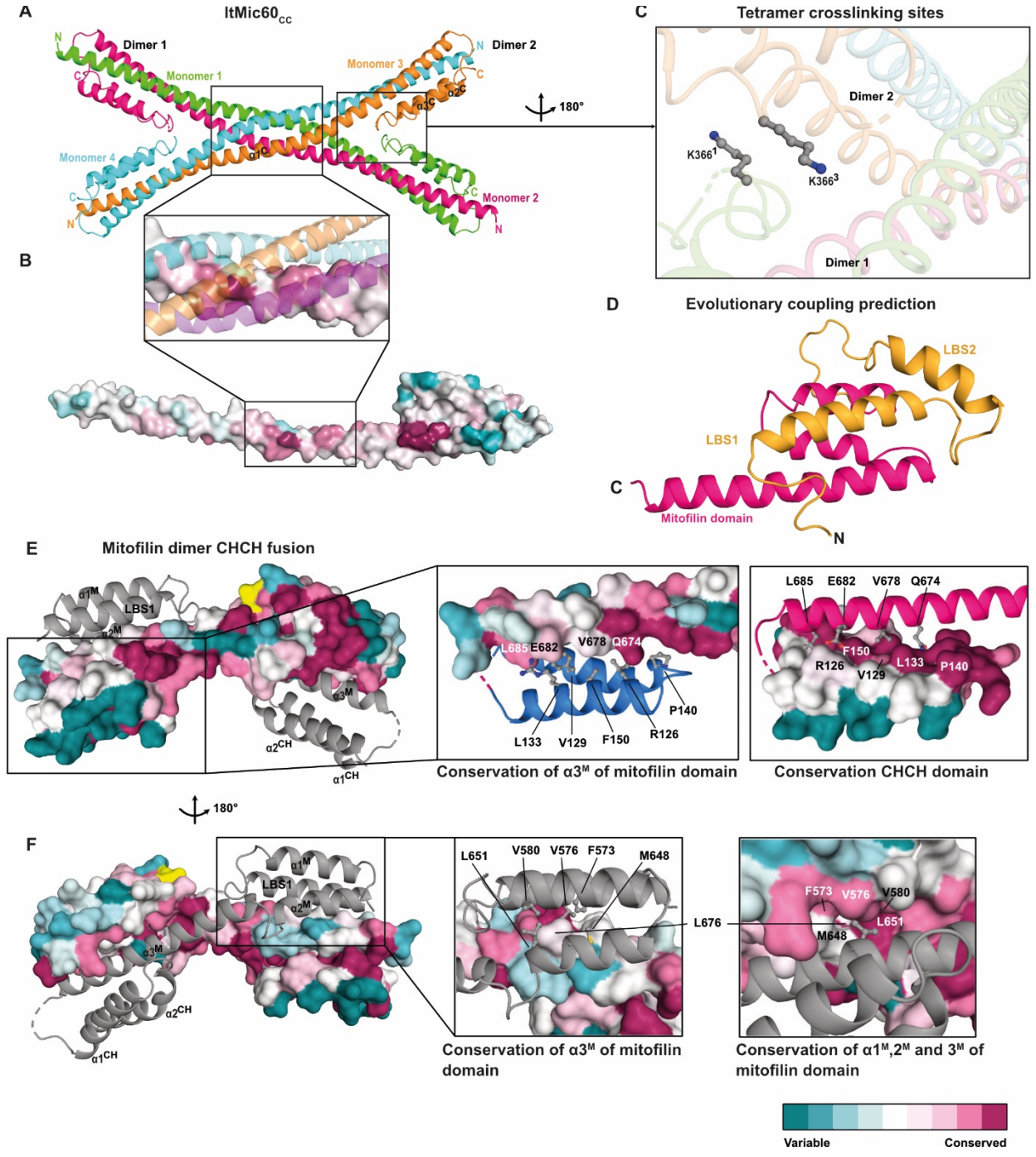

Fig. S3. Structural details of Mic60 and Mic19.

(A) Tetrameric structure of ltMic60CC. Tetrameric helical assemblies are often found in membrane-remodeling proteins, such as in SNARE complexes (*59*) or the stalks of dynamin proteins (*60*), although the detailed topologies differ. **(B)** Surface conservation plot of the tetramer interface (magnified area) and the monomer of ltMic60CC. The other monomers are shown in cartoon representation. Conserved residues are colored dark magenta, variable residues dark cyan. **(C)** Localization of K366, which was exchanged to cysteine to stabilize the tetramer via a disulfide bridge. $K366^1$ refers to monomer 1 and $K366^3$ to monomer 3. **(D)** Structure prediction of the C-

terminal region of Mic60 from co-evolution analysis. The mitofilin domain is colored in magenta and LBS 1/LBS 2 in orange. **(E), (F)** Surface conservation plot of one monomer of Mito2_CHCH. The second monomer is shown in cartoon representation. The GS-linker is colored in yellow. Both magnifications in **(E)** show the conservation of the mitofilin-CHCH domain interface. The CHCH domain or helix $\alpha 3^{M}$ from the mitofilin domain are displayed as cartoon representation for better visualization. The magnifications in **(F)** represent the conservation of the mitofilin-dimer interface.

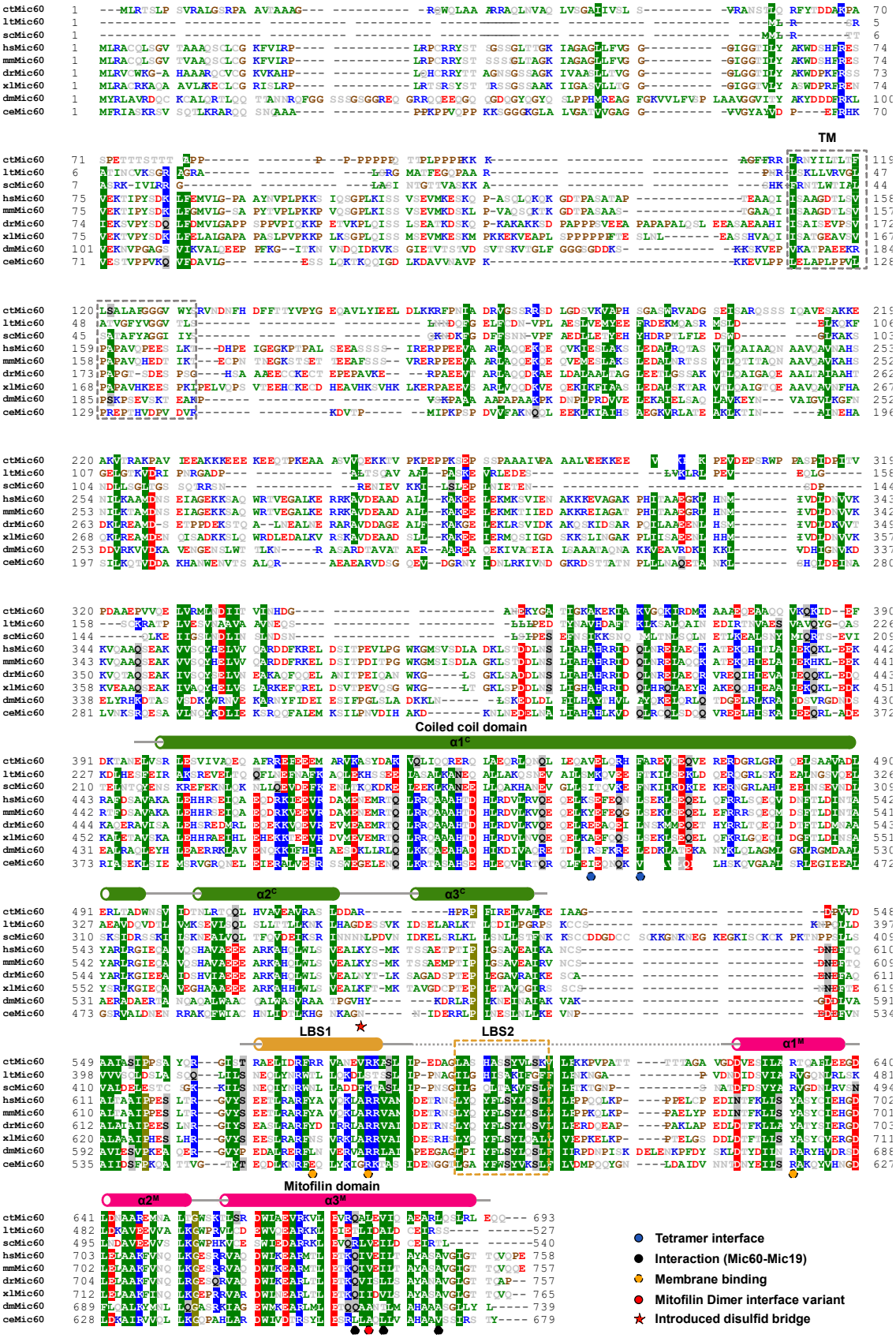

Fig. S4. Sequence alignment of Mic60.

Fig. S4. Sequence alignment of Mic60.

The following sequences are aligned: *Chaetomium thermophilum* (ctMic60, Uniprot accession code G0SHY5), *Lachancea thermotolerans* (ltMic60, C5E325), *Saccharomyces cerevisiae* (scMic60, P36112), *Homo sapiens* (hsMic60, Q16891), *Mus musculus* (mmMic60, Q8CAQ8), *Danio rerio* (drMic60, Q6PFS4), *Xenopus laevis* (xlMic60, A0A1L8HKP3), *Drosophila melanogaster* (dmMic60, P91928) *Caenorhabditis elegans* (ceMic60, Q22505). Amino acids are colored according to their chemical and physical properties (positive charge: blue, negative charge: red, hydrophobic: green, proline and glycine: brown, all others: grey). For sequence conservation greater than 70%, the background is highlighted. Residues involved in tetramerization are labeled with ●, in interaction with Mic19 with ●, in membrane binding with ●, in mitofilin dimerization with ● and the residue chosen for cysteine replacement with ★.

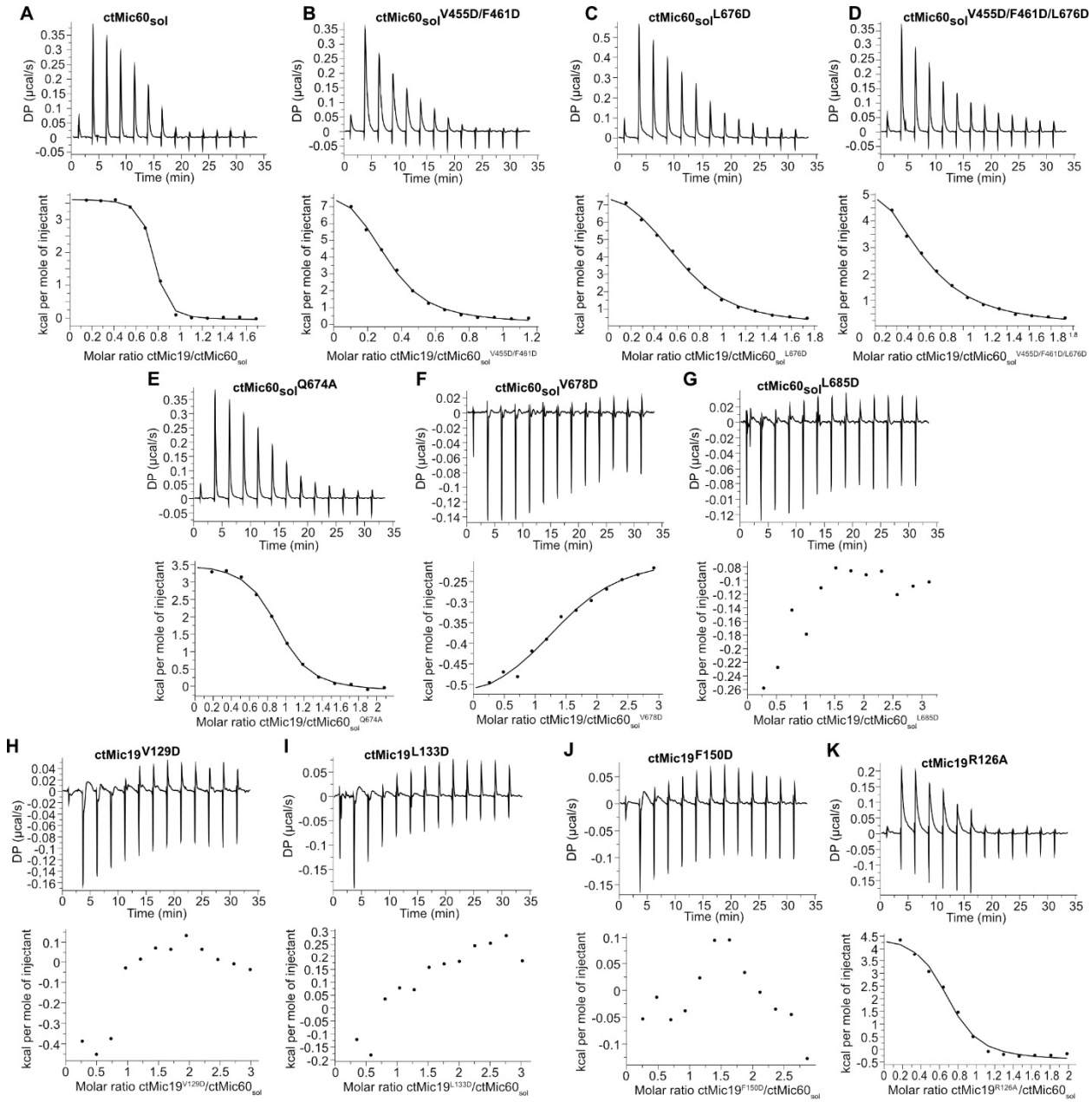

L

	K_D (µM)	Binding number
ctMic60$_{sol}$	0.19 ± 0.03	0.70 ± 0.01
ctMic60$_{sol}^{V455D/F461D}$	5 ± 1	0.30 ± 0.01
ctMic60$_{sol}^{L676D}$	6 ± 1	0.60 ± 0.02
ctMic60$_{sol}^{V455D/F461D/L676D}$	12 ± 3	0.42 ± 0.02
ctMic60$_{sol}^{Q674A}$	1.7 ± 0.2	0.87 ± 0.01
ctMic60$_{sol}^{V678D}$	11 ± 5	1.4 ± 0.1
ctMic60$_{sol}^{L685D}$	no binding	no binding

M

	K_D (µM)	Binding number
ctMic19	0.19 ± 0.03	0.70 ± 0.01
ctMic19^{R126A}	2.2 ± 0.7	0.65 ± 0.02
ctMic19^{V129D}	no binding	no binding
ctMic19^{L133D}	no binding	no binding
ctMic19^{F150D}	no binding	no binding

Fig. S5. ITC data of Mic60 and Mic19.

Fig. S5. ITC data for the interaction of Mic60 and Mic19.

(A-K) ITC experiments with different ctMic60$_{sol}$ variants and ctMic19 variants. At 10 °C, a concentrated solution of Mic19 in the syringe was titrated into a Mic60 solution present in the sample cell and the resulting heat change was monitored. Mic60 concentrations in the sample cell varied between 44-81 µM and Mic19 concentrations between 390-810 µM. **(L-M)** Overview of K_{DS} (µM) and binding numbers derived from the ITC experiments shown in **(A-K)**. The deviation represents the root-mean-square error of the fit. **(L)** includes the ctMic60$_{sol}$ variants, which have been titrated with ctMic19 and (**M**) the ctMic19 variants, which have been titrated into ctMic60$_{sol}$ solutions.

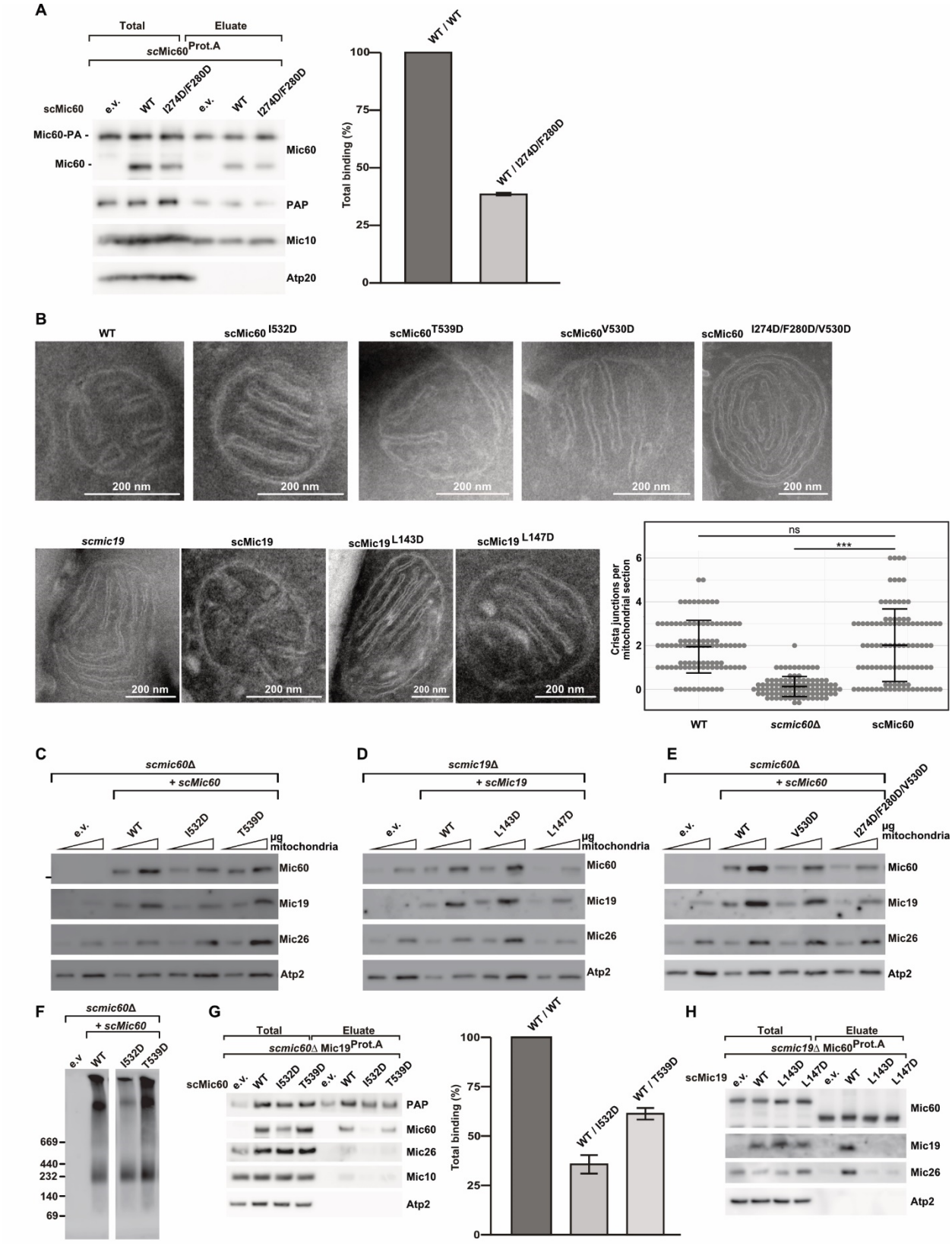

Fig. S6. *S. cerevisiae in vivo* analysis.

Fig. S6. *S. cerevisiae in vivo* analysis.

(A) Mitochondria harboring a chromosomally encoded Mic60-Protein A fusion construct together with plasmid-borne copies of either scMic60^{WT} or scMic60$^{I274D/F280D}$ were solubilized with digitonin and subjected to immunoprecipitation. After elution with glycine buffer, samples were analyzed by SDS-PAGE and Western blot (left panel). Quantification (right panel) of Mic60 antibody (for scMic60^{WT} and scMic60$^{I274D/F280D}$) and PAP (for Mic60-Protein A) signals demonstrates the reduced homotypic interaction propensity of scMic60$^{I274D/F280D}$ (n=4, data represent mean +- standard deviation). **(B)** Representative electron micrographs of *S. cerevisiae* mitochondria in ultrathin sections of cells expressing the indicated scMic60 and scMic19 variants. 'scMic19' represents the *mic19*Δ strain complemented with plasmid pRS416-scMic19 (WT) (see also Figs. 2E-G). Bottom right panel: number of crista junctions per mitochondrial section. 100 mitochondrial cross sections were counted with maximally two mitochondria from the same cell. Each data point represents one mitochondrial cross section, and mean and standard deviation are shown. Statistically significant differences in the mean values are indicated. **(C)** Comparison of steady state protein levels in isolated mitochondria of *S. cerevisiae* strains lacking the chromosomal *MIC60* gene (*mic60*Δ) transformed with an empty vector (e.v.), or plasmids encoding either wild-type (WT) scMic60 or the scMic60 variants I532D and T539D, respectively. Mitochondrial samples were subjected to SDS-PAGE and immunoblotting with the indicated antisera. Note that the I532D variant was expressed at lower levels compared to WT. **(D)** Protein steady state level analysis as in **(C)** using mitochondria of *S. cerevisiae* strains lacking Mic19 (*mic19*Δ) or expressing WT scMic19 or the scMic19 L143D or L147D variants, respectively. Note that the L147D variant was expressed at lower levels compared to WT. Accordingly, also lower levels of the MICOS components Mic60 and Mic26 were observed. **(E)** Experiment as described in **(C);** analyzed scMic60 variants were V530D and I274D/F280D/V530D. The Mic60 variant with three amino acid substitutions was expressed at slightly lower levels compared to WT. **(F)** Mitochondria as described in **(C)** additionally containing a Protein A-tagged variant of Mic19, were solubilized in digitonin-containing buffer and subjected to IgG affinity chromatography. Elution fractions were analyzed by blue native PAGE und immunodetection with antibodies raised against scMic60. **(G)** SDS-PAGE and Western blot analysis of immunoprecipitations with mitochondria lacking Mic60 *(mic60*Δ) or expressing Mic60 variants I532D and T539D in a scMic19-Protein A containing background. Quantification of PAP and scMic60 antibody signals shows different binding capacities of scMic60 variants to scMic19 compared to Mic60-WT (n=4, data represent mean +- standard deviation). **(H)** Mitochondria of yeast cells expressing scMic60-Protein A that either lack Mic19 *(*Δ*mic19*) or express scMic19^{L143D} or Mic19^{L147D} from plasmid pRS416 were subjected to immunoprecipitation. Samples were analyzed by SDS-PAGE and Western blot.

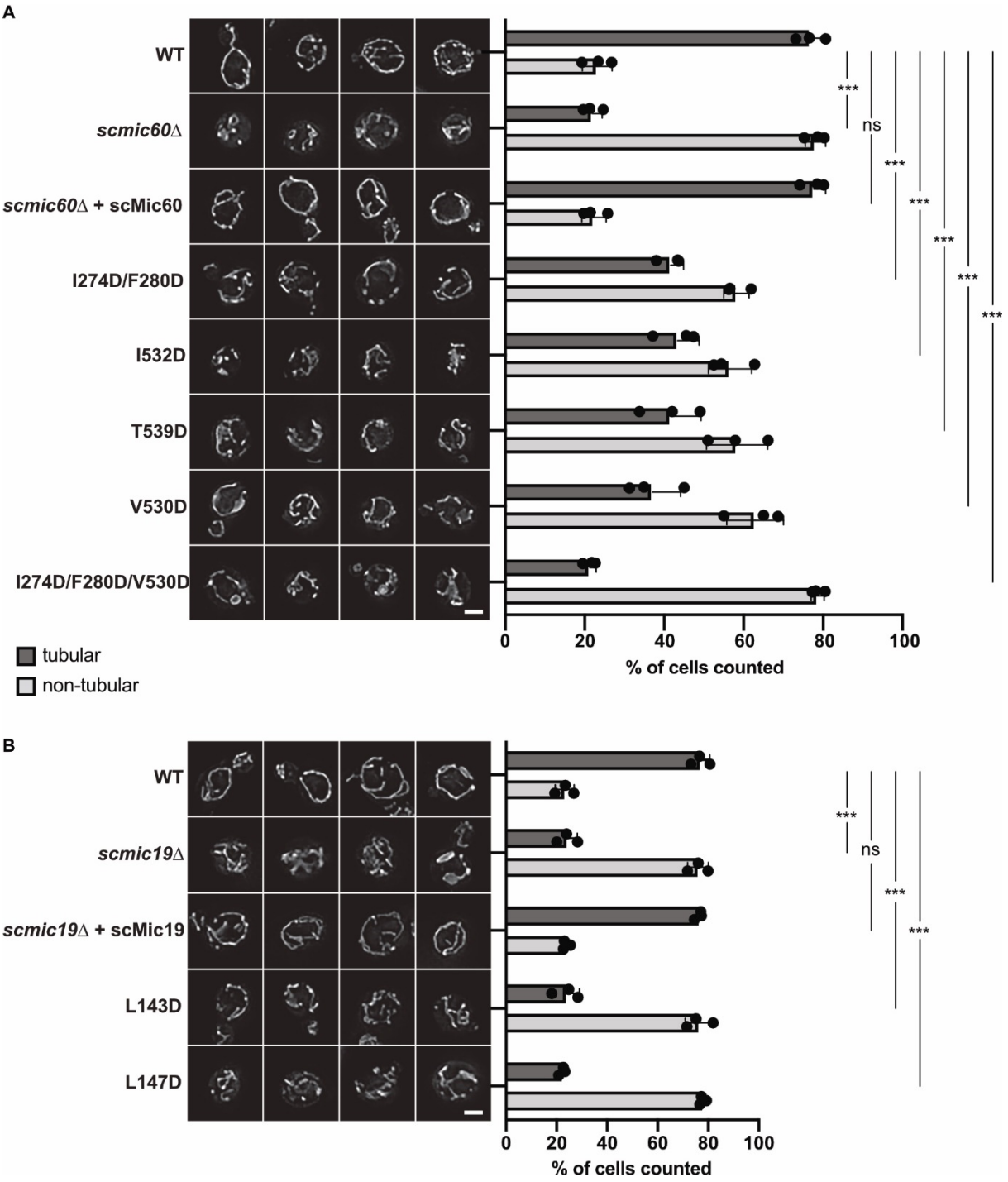

Fig. S7. Analysis of mitochondrial networks.

(**A**) Maximum projections of Z-stacks of mitochondrial stainings using 175 nM DiOC6 in wild-type (WT) *S. cerevisiae* and *MIC60* knockout cells containing either an empty plasmid or plasmids for the re-expression of WT-Mic60 ('rescue') or the indicated Mic60 variants, respectively. The bar diagram shows a quantitative analysis of mitochondrial networks from 3 independent experiments (black circles). About 300 cells were counted for each sample (p-values were derived from an unpaired t test). The white scale bar indicates 2 µm. (**B**) Same comparative analysis as in (**A**), but with cells harboring scMic19 variants.

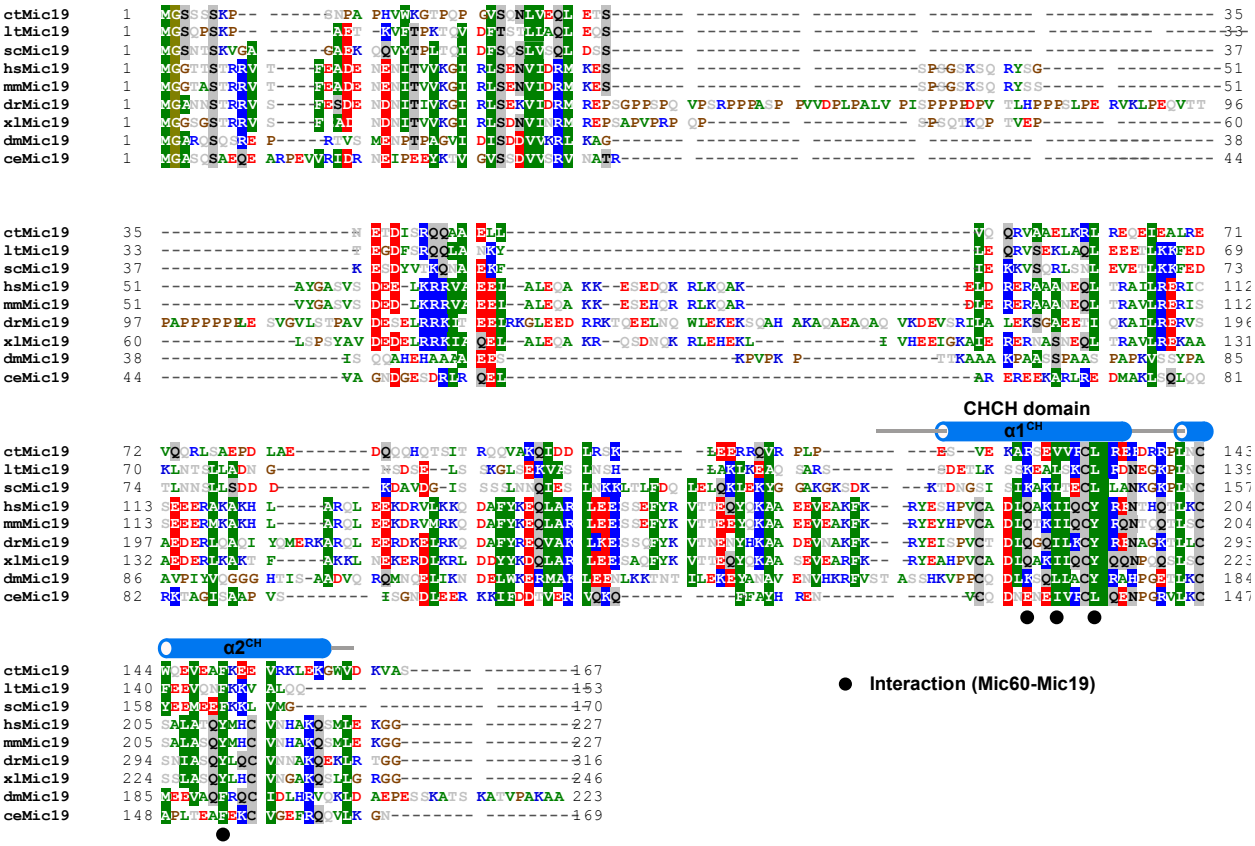

Fig. S8. Sequence alignment of Mic19.

The following sequences are aligned: *Chaetomium thermophilum* (ctMic19, Uniprot accession code G0S140), *Lachancea thermotolerans* (ltMic19, C5E3G4), *Saccharomyces cerevisiae* (scMic19, P43594), *Homo sapiens* (hsMic19, Q9NX63), *Mus musculus* (mmMic19, Q9CRB9), *Danio rerio* (drMic19, Q502T3), *Xenopus laevis* (xlMic19, Q7ZYP1), *Drosophila melanogaster* (dmMic19, Q9VA18), *Caenorhabditis elegans* (ceMic19, Q21551). Amino acids are colored according to their chemical and physical properties (positive charge: blue, negative charge: red, hydrophobic: green, proline and glycine: brown, all others: grey). For sequence conservation greater than 70%, the background is highlighted. Residues involved in interaction with Mic60 are labelled with ●.

Table S1. Crystallographic data collection and refinement statistics

	ltMic60$_{CC}$	Mito1_CHCH	Mito2_CHCH
Data collection			
Space group	$P42_12$	P1	$P2_1$
Cell dimensions			
a, *b*, *c* (Å)	54.2, 54.2, 134	43.82, 48.52, 70.74	58.20, 85.37, 61.50
α, β, γ (°)	90, 90, 90	82.70, 79.14, 72.41	90.00, 101.72, 90.00
Resolution (Å)	45-2.84 (3.01-2.84) *	46.12-2.15 (2.28-2.15) *	49.21-2.50 (2.65-2.50) *
R_{meas} (%)	16.8 (264)	9.0 (111.5)	13.0 (191.1)
$I / \sigma I$	13.1 (0.99)	8.28 (0.92)	9.16 (0.75)
Completeness (%)	99.7 (99)	91.8 (92.3)	98.8 (97.7)
Redundancy	13.5 (12.4)	2.5 (2.5)	4.0 (4.0)
CC(1/2) (%)	99.9 (76.0)	99.8 (52.9)	99.8 (39.4)
Refinement			
Resolution (Å)	44-2.84	46.12-2.15	40.74-2.50
No. reflections	5,157 (487)	27,211 (2,766)	20,337 (1,994)
R_{work} / R_{free} (%)	24.4 / 28.9	25.0 / 27.8	23.2 / 25.9
No. atoms			
Protein	1,127	3,693	4,394
Ligand/ion	0	36	39
Water	0	19	8
B-factors (Å^2)			
Protein	94.4	65.4	79.5
Ligand/ion	0	92.0	95.4
Water	0	44.3	58.9
R.m.s. deviations			
Bond lengths (Å)	0.003	0.003	0.003
Bond angles (°)	0.58	0.50	0.58
PDB accession code	7PUZ	7PV0	7PV1

* Data in highest resolution shell are indicated in parenthesis.

Table S2. Overview of Mic60 and Mic19 constructs.

Summary of all constructs used in this study. Lt: *Lachancea thermotolerans*, ct: *Chaetomium thermophilum*, sc: *Saccharomyces cerevisiae.*

ltMic60		ctMic60			scMic60			Comments
Boundaries	**Construct name**	**Boundaries**	**Mutations**	**Construct name**	**Boundaries**	**Mutations**	**Construct name**	
207-382	ltMic60cc							Crystallized coiled-coil domain
		208-691		$ctMic60_{sol}$	1-540		scMic60	Wild type protein
		208-691	V455D/F461D	$ctMic60_{sol}^{455D/F461D}$	1-540	I274D/F280D	$scMic60^{I274D/F280D}$	Broken tetramer interface
		208-691	L676D	$ctMic60_{sol}^{L676D}$	1-540	V530D	$scMic60^{V530D}$	Broken mitofilin dimer interface
		208-691	V455D/F461D/L676D	$ctMic60_{sol}^{V455D/F461D/L676D}$	1-540	I274D/F280D/V530D	$scMic60^{I274D/F280D/V530D}$	Broken tetramer and mitofilin dimer interface
		208-691	Q674A	$ctMic60_{sol}^{Q674A}$				Disturbed Mic60-Mic19 interaction
		208-691	V678D	$ctMic60_{sol}^{V679D}$	1-540	I532D	$scMic60^{I532D}$	Disturbed Mic60-Mic19 interaction
		208-691	L685D	$ctMic60_{sol}^{L685D}$	1-540	T539D	$scMic60^{T539D}$	Disturbed Mic60-Mic19 interaction
		208-691	R574D/R575D	$ctMic60_{sol}^{R574D/R575D}$				Reduced membrane binding
		208-691	R581D/K582D	$ctMic60_{sol}^{R581D/K582D}$				Reduced membrane binding
		208-691	R631D	$ctMic60_{sol}^{R631D}$				Reduced membrane binding
		ctMic19			**scMic19**			**Comments**
		Boundaries	**Mutations**	**Construct name**	**Boundaries**	**Mutations**	**Construct name**	
		1-164		ctMic19	1-170		scMic19	Wild type protein
		1-164	R126A	$ctMic19^{R126A}$				Disturbed Mic60-Mic19 interaction
		1-164	V129D	$ctMic19^{V129D}$	1-170	L143D	$scMic19^{L143D}$	Disturbed Mic60-Mic19 interaction
		1-164	L133D	$ctMic19^{L133D}$	1-170	L147D	$scMic19^{L147D}$	Disturbed Mic60-Mic19 interaction
		1-164	F150D	$ctMic19^{F150D}$				Disturbed Mic60-Mic19 interaction

Fusion proteins	**ctMic60**	**ctMic19**	**Mutation**	**Fusion protein**	**Comments**
Mito1_CHCH	624-691	116-164		$ctMic60^{624-691}$-GSGS-$ctMic19^{116-164}$	Crystallized mitofilin and CHCH domain
Mito2_CHCH	565-586-GS-622-691	116-164		$ctMic60^{565-586-GS-622-691}$-GSGS-$ctMic19^{116-164}$	Crystallized mitofilin-dimer and CHCH domain
$Mito2\_CHCH^{L676D}$	565-586-GS-622-691	116-164	L676D	$ctMic60^{565-586-GS-622-691}$-GSGS-$ctMic19^{116-164}$	Broken mitofilin domain dimer and CHCH domain

Table S3. Plasmids used in this study.

Plasmid	Description	Reference
pRS416	CEN, empty vector	Stratagene
pRS416-Mic60	CEN, Mic60	This study
pRS416-Mic60$^{I274D/F280D}$	CEN, Mic60$^{I274D/F280D}$	This study
pRS416-Mic60^{V530D}	CEN, Mic60^{V530D}	This study
pRS416-Mic60$^{I274D/F280D/V530D}$	CEN, Mic60$^{I274D/F280D/V530D}$	This study
pRS416-Mic60^{I532D}	CEN, Mic60^{I532D}	This study
pRS416-Mic60^{T539D}	CEN, Mic60^{T539D}	This study
pRS416-Mic19	CEN, Mic19	This study
pRS416-Mic19^{L143D}	CEN, Mic19^{L143D}	This study
pRS416-Mic19^{L147D}	CEN, Mic19^{L147D}	This study

CEN - Centromer

Table S4. *S. cerevisiae* strains used in this study.

Strain	Genotype	Reference
YPH499	WTMATa *ura3 lys2 ade2 trp1 his3 leu2*	Ref. 54
Δ*mic60*-pRS416	MATa *ura3 lys2 ade2 trp1 his3 leu2 MIC60::KanMX4* pRS416	This study
Δ*mic60*-Mic60	MATa *ura3 lys2 ade2 trp1 his3 leu2 MIC60::KanMX4* pRS416-Mic60	This study
Δ*mic60*-Mic60$^{I274D/F280D}$	MATa *ura3 lys2 ade2 trp1 his3 leu2 MIC60::KanMX4* pRS416-Mic60$^{I274D/F280D}$	This study
Δ*mic60*-Mic60^{V530D}	MATa *ura3 lys2 ade2 trp1 his3 leu2 MIC60::KanMX4* pRS416-Mic60 ^{V530D}	This study
Δ*mic60*-Mic60$^{I274D/F280D/V530D}$	MATa *ura3 lys2 ade2 trp1 his3 leu2 MIC60::KanMX4* pRS416-Mic60$^{I274D/F280D/V530D}$	This study
Δ*mic60*-Mic60^{I532D}	MATa *ura3 lys2 ade2 trp1 his3 leu2 MIC60::KanMX4* pRS416-Mic60 ^{I532D}	This study
Δ*mic60*-Mic60^{T539D}	MATa *ura3 lys2 ade2 trp1 his3 leu2 MIC60::KanMX4* pRS416-Mic60 ^{T539D}	This study
Δ*mic19*-pRS416	MATa *ura3 lys2 ade2 trp1 his3 leu2 MIC19::KanMX4* pRS416	This study
Δ*mic19*-Mic19	MATa *ura3 lys2 ade2 trp1 his3 leu2 MIC19::KanMX4* pRS416-Mic19	This study
Δ*mic19*-Mic19^{L143D}	MATa *ura3 lys2 ade2 trp1 his3 leu2 MIC19::KanMX4* pRS416-Mic19^{L143D}	This study
Δ*mic19*-Mic19^{L147D}	MATa *ura3 lys2 ade2 trp1 his3 leu2 MIC19::KanMX4* pRS416-Mic19^{L147D}	This study

Table S5. Antibodies used in this study.

Antibodies	Source	Identifier
anti-Atp2	Pfanner lab/ van der Laan lab	GR861
anti-Mic60	This study; amino acids 140-295	n/a
anti-Mic60	This study; amino acids 168-295	n/a
anti-Mic26	Pfanner lab/ van der Laan lab	GR3335
anti-Mic19	Pfanner lab/ van der Laan lab	GR3358

Movie S1 and S2. EM tomograms of crista junctions in fixed *S. cerevisiae*.

EM tomograms of mitochondria from *mic60*Δ *S. cerevisiae* reconstituted with Mic60 (Movie S1) or the Mic60 tetramerization mutant scMic60$^{I274D/F280D}$ (Movie S2). See also fig. S1C-F. Arrows point to the CJs.

REFERENCES AND NOTES

1. J. Nunnari, A. Suomalainen, Mitochondria: In sickness and in health. *Cell* **148**, 1145–1159 (2012).

2. R. J. Youle, Mitochondria-striking a balance between host and endosymbiont. *Science* **365**, eaaw9855 (2019).

3. D. C. Chan, Mitochondrial dynamics and its involvement in disease. *Annu. Rev. Pathol.* **15**, 235–259 (2020).

4. M. Giacomello, A. Pyakurel, C. Glytsou, L. Scorrano, The cell biology of mitochondrial membrane dynamics. *Nat. Rev. Mol. Cell Biol.* **21**, 204–224 (2020).

5. S. Schorr, M. van der Laan, Integrative functions of the mitochondrial contact site and cristae organizing system. *Semin. Cell Dev. Biol.* **76**, 191–200 (2018).

6. L. Colina-Tenorio, P. Horten, N. Pfanner, H. Rampelt, Shaping the mitochondrial inner membrane in health and disease. *J. Intern. Med.* **287**, 645–664 (2020).

7. K. M. Davies, C. Anselmi, I. Wittig, J. D. Faraldo-Gomez, W. Kuhlbrandt, Structure of the yeast F1Fo-ATP synthase dimer and its role in shaping the mitochondrial cristae. *Proc. Natl. Acad. Sci. U.S.A.* **109**, 13602–13607 (2012).

8. C. Glytsou, E. Calvo, S. Cogliati, A. Mehrotra, I. Anastasia, G. Rigoni, A. Raimondi, N. Shintani, M. Loureiro, J. Vazquez, L. Pellegrini, J. A. Enriquez, L. Scorrano, M. E. Soriano, Optic atrophy 1 is epistatic to the core MICOS component MIC60 in mitochondrial cristae shape control. *Cell Rep.* **17**, 3024–3034 (2016).

9. K. Faelber, L. Dietrich, J. K. Noel, F. Wollweber, A. K. Pfitzner, A. Mühleip, R. Sánchez, M. Kudryashev, N. Chiaruttini, H. Lilie, J. Schlegel, E. Rosenbaum, M. Hessenberger, C. Matthaeus, S. Kunz, A. von der Malsburg, F. Noé, A. Roux, M. van der Laan, W. Kühlbrandt, O. Daumke, Structure and assembly of the mitochondrial membrane remodelling GTPase Mgm1. *Nature* **571**, 429–433 (2019).

10. T. G. Frey, C. W. Renken, G. A. Perkins, Insight into mitochondrial structure and function from electron tomography. *Biochim. Biophys. Acta* **1555**, 196–203 (2002).

11. C. A. Mannella, Structure and dynamics of the mitochondrial inner membrane cristae. *Biochim. Biophys. Acta* **1763**, 542–548 (2006).

12. A. K. Kondadi, R. Anand, A. S. Reichert, Cristae membrane dynamics - A paradigm change. *Trends Cell Biol.* **30**, 923–936 (2020).

13. R. Rabl, V. Soubannier, R. Scholz, F. Vogel, N. Mendl, A. Vasiljev-Neumeyer, C. Körner, R. Jagasia, T. Keil, W. Baumeister, M. Cyrklaff, W. Neupert, A. S. Reichert, Formation of cristae and crista junctions in mitochondria depends on antagonism between Fcj1 and Su e/g. *J. Cell Biol.* **185**, 1047–1063 (2009).

14. M. Harner, C. Körner, D. Walther, D. Mokranjac, J. Kaesmacher, U. Welsch, J. Griffith, M. Mann, F. Reggiori, W. Neupert, The mitochondrial contact site complex, a determinant of mitochondrial architecture. *EMBO J.* **30**, 4356–4370 (2011).

15. S. Hoppins, S. R. Collins, A. Cassidy-Stone, E. Hummel, R. M. DeVay, L. L. Lackner, B. Westermann, M. Schuldiner, J. S. Weissman, J. Nunnari, A mitochondrial-focused genetic interaction map reveals a scaffold-like complex required for inner membrane organization in mitochondria. *J. Cell Biol.* **195**, 323–340 (2011).

16. K. von der Malsburg, J. M. Müller, M. Bohnert, S. Oeljeklaus, P. Kwiatkowska, T. Becker, A. Loniewska-Lwowska, S. Wiese, S. Rao, D. Milenkovic, D. P. Hutu, R. M. Zerbes, A. Schulze-Specking, H. E. Meyer, J. C. Martinou, S. Rospert, P. Rehling, C. Meisinger, M. Veenhuis, B. Warscheid, I. van der Klei, N. Pfanner, A. Chacinska, M. van der Laan, Dual role of mitofilin in mitochondrial membrane organization and protein biogenesis. *Dev. Cell* **21**, 694–707 (2011).

17. D. C. Jans, C. A. Wurm, D. Riedel, D. Wenzel, F. Stagge, M. Deckers, P. Rehling, S. Jakobs, STED super-resolution microscopy reveals an array of MINOS clusters along human mitochondria. *Proc. Natl. Acad. Sci. U.S.A.* **110**, 8936–8941 (2013).

18. T. Stephan, C. Brüser, M. Deckers, A. M. Steyer, F. Balzarotti, M. Barbot, T. S. Behr, G. Heim, W. Hübner, P. Ilgen, F. Lange, D. Pacheu-Grau, J. K. Pape, S. Stoldt, T. Huser, S. W. Hell, W. Möbius, P. Rehling, D. Riedel, S. Jakobs, MICOS assembly controls mitochondrial inner membrane remodeling and crista junction redistribution to mediate cristae formation. *EMBO J.* **39**, e104105 (2020).

19. M. Bohnert, R. M. Zerbes, K. M. Davies, A. W. Mühleip, H. Rampelt, S. E. Horvath, T. Boenke, A. Kram, I. Perschil, M. Veenhuis, W. Kühlbrandt, I. J. van der Klei, N. Pfanner, M. van der Laan, Central role of Mic10 in the mitochondrial contact site and cristae organizing system. *Cell Metab.* **21**, 747–755 (2015).

20. M. Barbot, D. C. Jans, C. Schulz, N. Denkert, B. Kroppen, M. Hoppert, S. Jakobs, M. Meinecke, Mic10 oligomerizes to bend mitochondrial inner membranes at cristae junctions. *Cell Metab.* **21**, 756–763 (2015).

21. V. Guarani, E. M. McNeill, J. A. Paulo, E. L. Huttlin, F. Fröhlich, S. P. Gygi, D. van Vactor, J. W. Harper, QIL1 is a novel mitochondrial protein required for MICOS complex stability and cristae morphology. *eLife* **4**, e06265 (2015).

22. J. R. Friedman, A. Mourier, J. Yamada, J. M. McCaffery, J. Nunnari, MICOS coordinates with respiratory complexes and lipids to establish mitochondrial inner membrane architecture. *eLife* **4**, e07739 (2015).

23. M. Hessenberger, R. M. Zerbes, H. Rampelt, S. Kunz, A. H. Xavier, B. Purfürst, H. Lilie, N. Pfanner, M. van der Laan, O. Daumke, Regulated membrane remodeling by Mic60 controls formation of mitochondrial crista junctions. *Nat. Commun.* **8**, 15258 (2017).

24. D. Tarasenko, M. Barbot, D. C. Jans, B. Kroppen, B. Sadowski, G. Heim, W. Möbius, S. Jakobs, M. Meinecke, The MICOS component Mic60 displays a conserved membrane-bending activity that is necessary for normal cristae morphology. *J. Cell Biol.* **216**, 889–899 (2017).

25. P. S. Tirrell, K. N. Nguyen, K. Luby-Phelps, J. R. Friedman, MICOS subcomplexes assemble independently on the mitochondrial inner membrane in proximity to ER contact sites. *J. Cell Biol.* **219**, (2020).

26. M. Bohnert, L. S. Wenz, R. M. Zerbes, S. E. Horvath, D. A. Stroud, K. von der Malsburg, J. M. Müller, S. Oeljeklaus, I. Perschil, B. Warscheid, A. Chacinska, M. Veenhuis, I. J. van der Klei, G. Daum, N. Wiedemann, T. Becker, N. Pfanner, M. van der Laan, Role of mitochondrial inner membrane organizing system in protein biogenesis of the mitochondrial outer membrane. *Mol. Biol. Cell* **23**, 3948–3956 (2012).

27. C. Ott, E. Dorsch, M. Fraunholz, S. Straub, V. Kozjak-Pavlovic, Detailed analysis of the human mitochondrial contact site complex indicate a hierarchy of subunits. *PLOS ONE* **10**, e0120213 (2015).

28. R. M. Zerbes, P. Hoss, N. Pfanner, M. van der Laan, M. Bohnert, Distinct roles of Mic12 and Mic27 in the mitochondrial contact site and cristae organizing system. *J. Mol. Biol.* **428**, 1485–1492 (2016).

29. T. A. Hopf, A. G. Green, B. Schubert, S. Mersmann, C. P. I. Schärfe, J. B. Ingraham, A. Toth-Petroczy, K. Brock, A. J. Riesselman, P. Palmedo, C. Kang, R. Sheridan, E. J. Draizen, C. Dallago, C. Sander, D. S. Marks, The EVcouplings Python framework for coevolutionary sequence analysis. *Bioinformatics* **35**, 1582–1584 (2019).

30. J. K. Pape, T. Stephan, F. Balzarotti, R. Büchner, F. Lange, D. Riedel, S. Jakobs, S. W. Hell, Multicolor 3D MINFLUX nanoscopy of mitochondrial MICOS proteins. *Proc. Natl. Acad. Sci. U.S.A.* **117**, 20607–20614 (2020).

31. C. Ott, K. Ross, S. Straub, B. Thiede, M. Götz, C. Goosmann, M. Krischke, M. J. Mueller, G. Krohne, T. Rudel, V. Kozjak-Pavlovic, Sam50 functions in mitochondrial intermembrane space bridging and biogenesis of respiratory complexes. *Mol. Cell. Biol.* **32**, 1173–1188 (2012).

32. F. Sadeqi, K. Stroh, M. Vache, D. Riedel, A. Janshoff, H. J. Risselada, M. Meinecke, Membrane interactions of mitochondrial lipid transfer proteins. bioRxiv 2022.04.05.487160 [Preprint]. 7 April 2022. https://doi.org/10.1101/2022.04.05.487160.

33. T. B. Blum, A. Hahn, T. Meier, K. M. Davies, W. Kuhlbrandt, Dimers of mitochondrial ATP synthase induce membrane curvature and self-assemble into rows. *Proc. Natl. Acad. Sci. U.S.A.* **116**, 4250–255 (2019).

34. H. Rampelt, F. Wollweber, M. Licheva, R. de Boer, I. Perschil, L. Steidle, T. Becker, M. Bohnert, I. van der Klei, C. Kraft, M. van der Laan, N. Pfanner, Dual role of Mic10 in mitochondrial cristae organization and ATP synthase-linked metabolic adaptation and respiratory growth. *Cell Rep.* **38**, 110290 (2022).

35. C. Zhu, J. Wu, H. Sun, F. Briganti, B. Meder, W. Wei, L. M. Steinmetz, Single-molecule, full-length transcript isoform sequencing reveals disease-associated RNA isoforms in cardiomyocytes. *Nat. Commun.* **12**, 4203 (2021).

36. B. B. Hulsmann, A. A. Labokha, D. Gorlich, The permeability of reconstituted nuclear pores provides direct evidence for the selective phase model. *Cell* **150**, 738–751 (2012).

37. H. Liu, J. H. Naismith, An efficient one-step site-directed deletion, insertion, single and multiple-site plasmid mutagenesis protocol. *BMC Biotechnol.* **8**, 91 (2008).

38. R. Chalk, Mass spectrometric analysis of proteins. *Methods Mol. Biol.* **1586**, 373–395 (2017).

39. U. Mueller, R. Förster, M. Hellmig, F. U. Huschmann, A. Kastner, P. Malecki, S. Pühringer, M. Röwer, K. Sparta, M. Steffien, M. Ühlein, P. Wilk, M. S. Weiss, The macromolecular crystallography beamlines at BESSY II of the Helmholtz-Zentrum Berlin: Current status and perspectives. *Eur. Phys. J. Plus* **130**, 141 (2015).

40. K. M. Sparta, M. Krug, U. Heinemann, U. Mueller, M. S. Weiss, XDSAPP2.0. *J. Appl. Crystallogr.* **49**, 1085–1092 (2016).

41. M. D. Winn, C. C. Ballard, K. D. Cowtan, E. J. Dodson, P. Emsley, P. R. Evans, R. M. Keegan, E. B. Krissinel, A. G. W. Leslie, A. McCoy, S. J. McNicholas, G. N. Murshudov, N. S. Pannu, E. A. Potterton, H. R. Powell, R. J. Read, A. Vagin, K. S. Wilson, Overview of the CCP_4 suite and current developments. *Acta Crystallogr. D Biol. Crystallogr.* **67**, 235–242 (2011).

42. J. Bibby, R. M. Keegan, O. Mayans, M. D. Winn, D. J. Rigden, AMPLE: A cluster-and-truncate approach to solve the crystal structures of small proteins using rapidly computed ab initio models. *Acta Crystallogr. D Biol. Crystallogr.* **68**, 1622–1631 (2012).

43. D. Liebschner, P. V. Afonine, M. L. Baker, G. Bunkóczi, V. B. Chen, T. I. Croll, B. Hintze, L. W. Hung, S. Jain, A. J. McCoy, N. W. Moriarty, R. D. Oeffner, B. K. Poon, M. G. Prisant, R. J. Read, J. S. Richardson, D. C. Richardson, M. D. Sammito, O. V. Sobolev, D. H. Stockwell, T. C. Terwilliger, A. G. Urzhumtsev, L. L. Videau, C. J. Williams, P. D. Adams, Macromolecular structure determination using x-rays, neutrons and electrons: Recent developments in Phenix. *Acta Crystallogr. D Struct. Biol.* **75**, 861–877 (2019).

44. T. C. Terwilliger, R. W. Grosse-Kunstleve, P. V. Afonine, N. W. Moriarty, P. H. Zwart, L. W. Hung, R. J. Read, P. D. Adams, Iterative model building, structure refinement and density modification with the PHENIX auto buildwizard. *Acta Crystallogr. D Biol. Crystallogr.* **64**, 61–69 (2008).

45. A. J. McCoy, R. W. Grosse-Kunstleve, P. D. Adams, M. D. Winn, L. C. Storoni, R. J. Read, Phaser crystallographic software. *J. Appl. Cryst.* **40**, 658–674 (2007).

46. G. M. Sheldrick, A short history of SHELX. *Acta Crystallogr. A* **64**, 112–122 (2008).

47. P. Emsley, B. Lohkamp, W. G. Scott, K. Cowtan, Features and development of Coot. *Acta Crystallogr. D Biol. Crystallogr.* **66**, 486–501 (2010).

48. P. V. Afonine, R. W. Grosse-Kunstleve, N. Echols, J. J. Headd, N. W. Moriarty, M. Mustyakimov, T. C. Terwilliger, A. Urzhumtsev, P. H. Zwart, P. D. Adams, Towards automated crystallographic structure refinement with phenix.refine. *Acta Crystallogr. D Biol. Crystallogr.* **68**, 352–367 (2012).

49. C. J. Williams, J. J. Headd, N. W. Moriarty, M. G. Prisant, L. L. Videau, L. N. Deis, V. Verma, D. A. Keedy, B. J. Hintze, V. B. Chen, S. Jain, S. M. Lewis, W. B. Arendall III, J. Snoeyink, P. D. Adams, S. C. Lovell, J. S. Richardson, D. C. Richardson, MolProbity: More and better reference data for improved all-atom structure validation. *Protein Sci.* **27**, 293–315 (2018).

50. H. Ashkenazy, S. Abadi, E. Martz, O. Chay, I. Mayrose, T. Pupko, N. Ben-Tal, ConSurf 2016: An improved methodology to estimate and visualize evolutionary conservation in macromolecules. *Nucleic Acids Res.* **44**, W344–W350 (2016).

51. E. Krissinel, K. Henrick, Inference of macromolecular assemblies from crystalline state. *J. Mol. Biol.* **372**, 774–797 (2007).

52. C. A. Schneider, W. S. Rasband, K. W. Eliceiri, NIH image to imageJ: 25 years of image analysis. *Nat. Methods* **9**, 671–675 (2012).

53. P. Schuck, Size-distribution analysis of macromolecules by sedimentation velocity ultracentrifugation and lamm equation modeling. *Biophys. J.* **78**, 1606–1619 (2000).

54. R. S. Sikorski, P. Hieter, A system of shuttle vectors and yeast host strains designed for efficient manipulation of DNA in *Saccharomyces cerevisiae*. *Genetics* **122**, 19–27 (1989).

55. M. Knop, K. Siegers, G. Pereira, W. Zachariae, B. Winsor, K. Nasmyth, E. Schiebel, Epitope tagging of yeast genes using a PCR-based strategy: More tags and improved practical routines. *Yeast* **15**, 963–972 (1999).

56. J. W. Slot, H. J. Geuze, Cryosectioning and immunolabeling. *Nat. Protoc.* **2**, 2480–2491 (2007).

57. K. T. Tokuyasu, A technique for ultracryotomy of cell suspensions and tissues. *J. Cell Biol.* **57**, 551–565 (1973).

58. D. N. Mastronarde, S. R. Held, Automated tilt series alignment and tomographic reconstruction in IMOD. *J. Struct. Biol.* **197**, 102–113 (2017).

59. R. B. Sutton, D. Fasshauer, R. Jahn, A. T. Brunger, Crystal structure of a SNARE complex involved in synaptic exocytosis at 2.4 A resolution. *Nature* **395**, 347–353 (1998).

60. S. Gao, A. von der Malsburg, S. Paeschke, J. Behlke, O. Haller, G. Kochs, O. Daumke, Structural basis of oligomerization in the stalk region of dynamin-like MxA. *Nature* **465**, 502–506 (2010).